

Promoting ordering degree of intermetallic fuel cell catalysts by low-melting-point metal doping

Received: 9 February 2023

Accepted: 11 September 2023

Published online: 22 September 2023

Check for updates

Ru-Yang Shao^{1,4}, Xiao-Chu Xu^{2,4}, Zhen-Hua Zhou², Wei-Jie Zeng², Tian-Wei Song², Peng Yin¹, Ang Li², Chang-Song Ma², Lei Tong^{1,2}, Yuan Kong^{1,3} & Hai-Wei Liang^{1,2}

Carbon supported intermetallic compound nanoparticles with high activity and stability are promising cathodic catalysts for oxygen reduction reaction in proton-exchange-membrane fuel cells. However, the synthesis of intermetallic catalysts suffers from large diffusion barrier for atom ordering, resulting in low ordering degree and limited performance. We demonstrate a low-melting-point metal doping strategy for the synthesis of highly ordered L1₀-type M-doped PtCo (M = Ga, Pb, Sb, Cu) intermetallic catalysts. We find that the ordering degree of the M-doped PtCo catalysts increases with the decrease of melting point of M. Theoretic studies reveal that the low-melting-point metal doping can decrease the energy barrier for atom diffusion. The prepared highly ordered Ga-doped PtCo catalyst exhibits a large mass activity of 1.07 A mg_{Pt}⁻¹ at 0.9 V in H₂-O₂ fuel cells and a rated power density of 1.05 W cm⁻² in H₂-air fuel cells, with a Pt loading of 0.075 mg_{Pt} cm⁻².

Proton-exchange membrane fuel cells (PEMFCs) are considered widely as promising renewable energy applications in response to the target of “carbon neutrality” owing to their high energy conversion efficiency and zero-emission¹. Currently, the commercial PEMFCs stacks rely heavily on carbon-supported platinum (Pt/C) or PtCo alloy catalysts^{2,3}. For future large-scale commercialization, a key developmental target of PEMFCs is to reduce the loading of platinum-group-metal to less than 0.10 g/kW⁴. However, as the content of platinum in the catalyst layer decreases, increased voltage loss inevitably arises, leading to poor PEMFCs performance from the efficiency point of view⁵. To this end, advanced Pt-alloy catalysts with smaller activation polarization voltage loss have been explored because of their higher mass-based activity, which can compensate for the voltage loss in the high potential region for the low-Pt cathode^{2,5,6}. The improved electrocatalytic activity of Pt-alloys (e.g., PtCo, PtNi) relative to Pt/C was often ascribed to the compressive strain effect that is associated with the smaller Pt-Pt distance in Pt shells of alloy catalysts, which would weaken the binding energy of oxygen-containing intermediate

species (E_o) and thus promote the oxygen reduction reaction (ORR) kinetics^{7–9}.

Compared to random alloys, atomically ordered intermetallic compounds (IMCs), especially the tetragonal distortion of random PtCo with atom ratio of 1:1 (L1₀-type), have attracted increasing attention due to their more compressive unit cells and larger formation enthalpy that endow IMCs catalysts with enhanced ORR activity and durability^{9–16}. Recently, it has been experimentally verified that the ORR activity was positively correlated with the ordering degree of the alloy catalysts^{17–20}, but the ordering degree of most reported so-called “intermetallic” catalysts was considerably low, especially for the ones prepared by the industry-relevant impregnation method^{10,18,21}. The challenge of preparing highly ordered IMCs catalysts is fundamentally associated with the competition between the thermodynamic driving force and the height of kinetic energy barriers for the disorder-to-order transition²². While lowering the annealing temperature far away from the critical temperature of phase transition (T_c) will increase the thermodynamic driving force for the nucleation of ordered phase in

¹Hefei National Research Center for Physical Sciences at the Microscale, University of Science and Technology of China, Hefei, China. ²Department of Chemistry, University of Science and Technology of China, Hefei, China. ³Department of Chemical Physics, University of Science and Technology of China, Hefei, China. ⁴These authors contributed equally: Ru-Yang Shao, Xiao-Chu Xu. e-mail: kongyuan@ustc.edu.cn; hwliang@ustc.edu.cn

disordered solid solution, the low-temperature annealing is detrimental to the atom diffusion. The trade-off between nucleation and diffusion with annealing temperature inevitably leads to the sluggish rate of disorder-to-order transition (Fig. 1a).

Here, we demonstrate a low-melting-point metal doping strategy to promote the atom diffusion rate, for the preparation of highly ordered $L1_0$ -type M-doped PtCo (M-PtCo, M = Ga, Pb, Sb, Cu for doped catalysts; M = Co for undoped PtCo) IMCs catalysts (Fig. 1a). We identify a strong dependence of ordering degree of the M-PtCo catalysts on the melting point of M: the ordering degree of the prepared catalysts increases gradually from -17% for the undoped PtCo to 65% for Ga-PtCo. Theoretic calculations confirm that the substitution of Co atoms in PtCo with low-melting-point metal atoms can significantly decrease the height of energy barrier for atom diffusion and thus promote the ordering degree. We note that the low-melting-point metals doping has been reported for the low-temperature preparation of intermetallic materials in the field of magnetism^{23–26}. The prepared highly ordered Ga-PtCo IMCs catalysts deliver enhanced ORR activity compared to the undoped PtCo catalysts with lower ordering degree. In particular, the Ga-PtCo IMCs catalysts show a high mass activity of $1.07 \text{ A mg}_{\text{Pt}}^{-1}$ at $0.9 V_{\text{IR-corrected}}$ in H_2 - O_2 fuel cells, along with only 17.8% loss after the accelerated durability tests. The low-melting-point metal doping strategy is also effective for the preparation of Ga-doped PtFe and PtNi IMCs catalysts with improved ordering degree.

Results

Structure characterization of M-PtCo (M = Ga, Pb, Sb, Cu)

Carbon-supported M-PtCo (M = Ga, Pb, Sb, Cu) precursors were obtained by the wet-impregnation of corresponding metal salts onto the carbon black Ketjenblack EC-600JD (KJ600) support with a total metal content of 20 wt% and Pt/Co/M atomic ratio of 1:0.8:0.2, which were then subjected to annealing treatment at 1000°C under 5 vol% H_2/Ar . Undoped PtCo with Pt/Co atomic ratio of 1:1 was also prepared for comparison. X-ray diffraction (XRD) patterns showed that the characteristic reflections of the as-prepared M-PtCo matched well with the ordered $L1_0$ -PtCo intermetallic phase (Fig. 1b). The average crystallite size is estimated to be around 4 nm for all the M-PtCo catalysts by the Debye-Scherrer equation based on the full width at half

maximum of XRD patterns (Table S1). High-angle annular dark-field scanning transmission electron microscopy (HAADF-STEM) observations showed that numerous M-PtCo nanoparticles were uniformly dispersed throughout the carbon supports with similar average particle size (Fig. 1c). Statistical analyses of particle size distribution from the low-magnification HAADF-STEM images were consistent well with the XRD results (Figure S1, S2, and Table S1). Elemental mapping with energy-dispersive x-ray spectroscopy (EDS) indicated that Pt and non-Pt elements were distributed homogeneously in individual M-PtCo nanoparticles with an atomic percent approximately equivalent to the theoretical value (Figures S3–S5 and Table S2).

After subtracting the background, the XRD patterns were analyzed further to quantify the ordering degree (Fig. 1b and Figure S6, see the Methods section for the calculation details of the ordering degree)¹⁸. The ordering degree of the IMCs catalysts increased from $16.36 \pm 5.52\%$ for undoped PtCo to $22.39 \pm 5.28\%$ for Cu-PtCo, $34.76 \pm 8.04\%$ for Sb-PtCo, $47.06 \pm 5.78\%$ for Pb-PtCo, and $65.33 \pm 2.67\%$ for Ga-PtCo (Table S3). Specifically, the (111) diffraction peak gradually shifted to the position of almost fully ordered $L1_0$ structure with the increase of ordering degree (Figure S7). We further identified that the ordering degree of the M-PtCo catalysts increased with the decrease of the melting point of M (Fig. 1d). Since all the catalysts showed similar crystallite size, the influence of size-dependent thermodynamic drive force of disorder-to-order transition on the ordering degree could be excluded^{27–29}.

Mechanism of melting point-dependent ordering degree

To gain insight into the mechanism of the melting point-dependent ordering degree for the M-PtCo catalysts, we performed Density Functional Theory (DFT) calculations to analyze the influence of metal doping on the disorder-to-order transition from the perspectives of both thermodynamics and kinetics. The structural model was constrained by crystal symmetry and a 1/8 doped-PtCo model was used. We assumed that the disorder-to-order transition could be achieved by sliding atoms of adjacent layers (Figure S8). The DFT calculations revealed that there was a clear downward trend in the diffusion potential of M-PtCo, with the energy barrier order of $\text{Co} (8.36 \text{ eV}) > \text{Cu} (5.98 \text{ eV}) > \text{Sb} (5.76 \text{ eV}) > \text{Ga} (5.55 \text{ eV}) > \text{Pb} (5.41 \text{ eV})$, although the

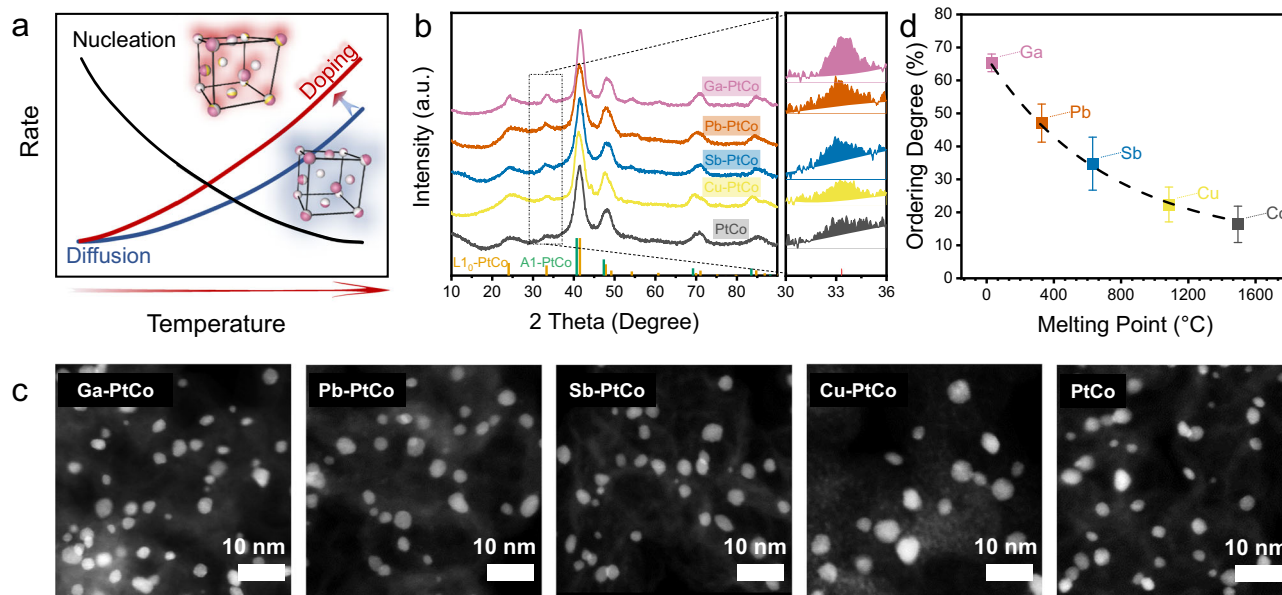


Fig. 1 | Structural characterization of M-PtCo NPs. **a** Schematic illustration showing the dependence of nucleation and diffusion kinetic rate on temperature in the disorder-to-order transition. **b** XRD patterns of M-PtCo (M = Co, Cu, Sb, Pb, Ga), with the highlighted super lattice peak at around 32.8° . The standard peaks for $A1$

and $L1_0$ PtCo are also shown. **c** HAADF-STEM images of M-PtCo. **d** Ordering degree of the M-PtCo catalysts versus melting point of M. The error bars were obtained by three parallel experiments.

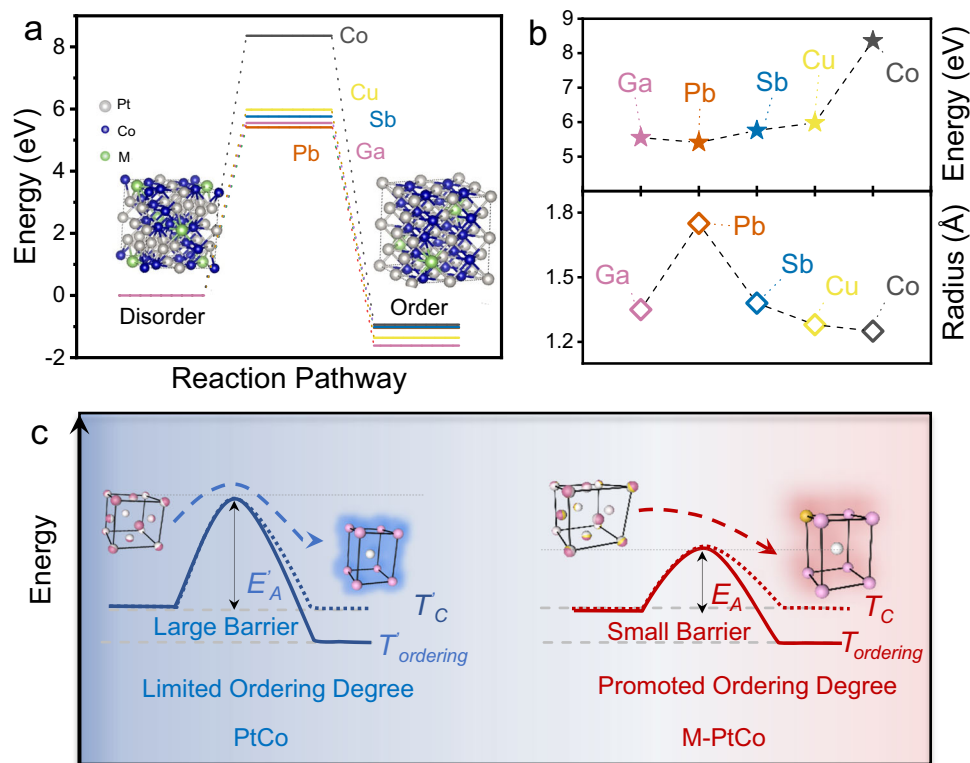


Fig. 2 | Mechanism of melting-point dependent ordering degree of M-PtCo. **a** DFT calculation showing the decreased energy barrier of disorder-order phase transition with the low-melting-point metal doping. The insets are the atomic

model for disordered and ordered M-PtCo. **b** Phase transition energy barrier of M-PtCo and atom radius of M. **c** Schematic illustration showing the smaller barrier of disorder-to-order transition for M-PtCo compared to PtCo.

driving force of the phase transition was not much affected by the doped metal (Fig. 2a, b). This result is consistent with the experimental conclusion except for Pb-PtCo. We find that the atomic radii of the other elements are between Co (125 pm) and Pt (139 pm), while the radius of Pb is much larger (175 pm) (Fig. 2b). The larger atomic radius of Pb will lead to increased steric hindrance for the interlayer atomic sliding in the phase transition process^{30,31}, and therefore suppress the disorder-to-order transition.

On the basis of the above experimental and theoretical studies, we figured out that the promoted ordering degree of the M-PtCo catalysts was associated with the significantly decreased energy barrier of atom diffusion that was induced by the low-melting-metal doping (Fig. 2c). The annealing at a relatively high temperature (i.e., 1000 °C) could ensure the rapid atom diffusion across the support to form well-alloyed but disordered M-PtCo, and the nucleation of ordered L₁₀-M-PtCo would occur once the sample was cooled to below the critical temperature of phase transition (T_c)^{20,32}. Further decreasing the temperature far away from T_c could get a larger thermodynamic driving force for the formation of L₁₀-M-PtCo seeds but slow down the atom diffusion. At a certain temperature ($T_{ordering}$) below T_c , the diffusion rate of the disorder-to-order transition was dependent on the difference between diffusion barrier (E_A) and the driven force for atom diffusion at $T_{ordering}$. Considering the significantly decreased diffusion barrier upon the low-melting-point metal doping, the diffusion rate in M-PtCo would be larger than that in undoped PtCo, which led to a faster disorder-to-order phase transition in M-PtCo.

Synthesis of highly ordered IMCs catalysts

To illustrate the universality of the low-melting-point metal doping strategy for the synthesis of highly ordered IMCs catalysts, Ga-doped L₁₀-PtFe (Ga-PtFe) and L₁₀-PtNi (Ga-PtNi) were also prepared (Figures S9a and S9b). The ordering degree of Ga-PtFe was 84% and much higher than that of undoped PtFe (26%). The undoped PtNi was

completely disordered structure. The difficulty of obtaining ordered PtNi structure lies in its low T_c (-630 °C), which makes it challenging to balance the trade-off between nucleation and atom diffusion. With the Ga doping, we got the partially ordered Ga-PtNi catalyst with an ordering degree of 30%.

For electrochemical studies, the Ga-PtCo catalyst with a lower Ga/Co atomic ratio of 1:9 (denoted as Ga_{0.1}-PtCo) was also prepared in addition to the common one with Ga/Co atomic ratio of 2:8 (denoted as Ga-PtCo). XRD and HAADF-STEM analyses revealed that the prepared Ga_{0.1}-PtCo catalyst had similar ordering degree (62%) and average particle size (3.57 nm) to that of Ga-PtCo (Fig. 3a, b). Cs-corrected HAADF-STEM was used to analyze the atomic ordered structure. The alternating arrangement of the brighter dots and darker dots observed along the [1-10] direction represents Pt and Co atom columns, respectively, indicating the L₁₀-type intermetallic structure (Fig. 3c, e, and Figure S10). Prior to electrochemical tests, the as-prepared Ga-doped PtCo catalysts were treated with 0.1 M HClO₄ at 60 °C for 1 h and then annealed at 400 °C for 2 h under Ar/H₂ atmosphere to form a highly stable core/shell structures consisting of an intermetallic core and a Pt shell^{10,33}. We found that the retention of alloying and ordering degree for the low-Ga-content catalyst (that is, Ga_{0.1}-PtCo) was higher than that for the high-Ga-content catalyst (that is, Ga-PtCo) after the acid leaching treatment (Figure S11 and Table S2). The superior structural stability of Ga_{0.1}-PtCo over Ga-PtCo was probably owing to the much lower dissolution potential of Ga (-0.549 V) compared to Pt (1.18 V) and Co (-0.28 V)^{34,35}. Spherical aberration (Cs)-corrected HAADF-STEM observations revealed that the post-treated Ga_{0.1}-PtCo catalyst had a core/shell structure composed of an L₁₀ PtCo core and a three-atom-layer Pt shell (Fig. 3d, f). EDS mapping showed that the atomic ratio of Pt: Co of Ga_{0.1}-PtCo changed from 1: 0.8: 0.082 to 1: 0.6: 0.019 after acid leaching, which was consistent with the inductively coupled plasma-atomic emission spectrometry (ICP-AES) results (Figure S12 and Table S2). However, severe leaching of Co and Ga was

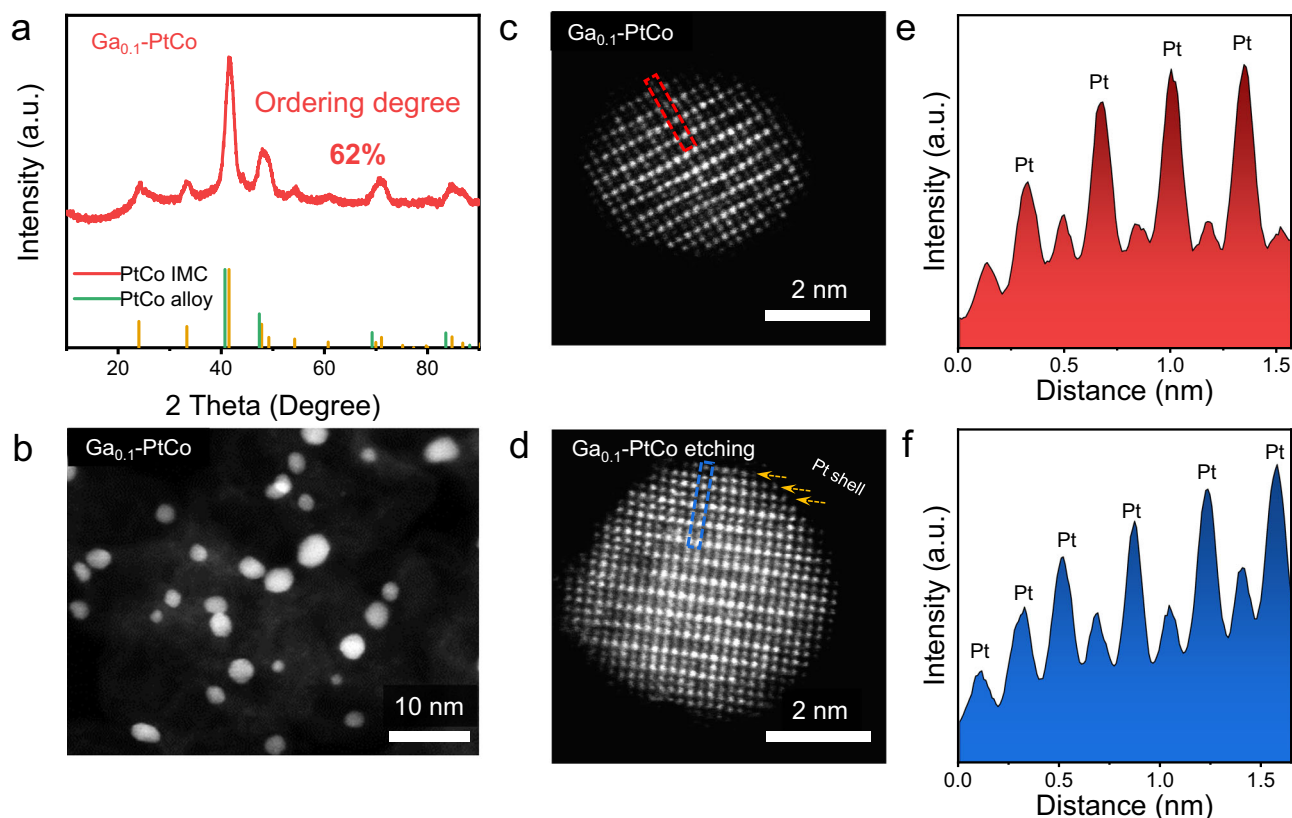


Fig. 3 | Synthesis and characterization of $L1_0$ $Ga_{0.1}$ -PtCo. **a** XRD pattern of $Ga_{0.1}$ -doped $L1_0$ PtCo. **b** HAADF-STEM image of $Ga_{0.1}$ -PtCo NPs. **c, d** Atomic-resolution HAADF-STEM images of untreated $Ga_{0.1}$ -PtCo NPs and post-treated $Ga_{0.1}$ -PtCo, respectively. **e, f** HAADF line profiles of the marked region in **c, d**.

found for the Ga-PtCo catalyst, in which only 57% Co and 16% Ga were retained after acid leaching.

Electrochemical performance

We studied the electrocatalytic performance of the treated Ga-PtCo catalysts for ORR by the rotating disk electrode (RDE) and membrane electrode assemblies (MEA) techniques. Undoped PtCo and commercial Pt/C (30 wt%, TKK) were also tested under the same conditions for comparison. Figure 4a displayed the RDE polarization curves of $Ga_{0.1}$ -PtCo, Ga-PtCo, PtCo, and commercial Pt/C in O_2 -saturated 0.1M $HClO_4$. The mass activity (MA) at 0.9 V_{RHE} of $Ga_{0.1}$ -PtCo was calculated to be $2.82 \pm 0.23 \text{ A mg}_{Pt}^{-1}$, which is higher than $2.30 \pm 0.07 \text{ A mg}_{Pt}^{-1}$ for Ga-PtCo, $1.45 \pm 0.03 \text{ A mg}_{Pt}^{-1}$ for PtCo, and $0.40 \pm 0.05 \text{ A mg}_{Pt}^{-1}$ for commercial Pt/C. The electrochemical surface areas (ECSA) were quantified to be $41.0 \pm 1.3 - 48.7 \pm 2.1 \text{ m}^2 \text{ g}_{Pt}^{-1}$ for the alloy catalysts by the CO stripping technique, which were lower than that of Pt/C ($69.1 \pm 0.67 \text{ m}^2 \text{ g}_{Pt}^{-1}$) (Figures S13 and S14). The lower ECSA of the alloy catalysts was associated to their broader particle size distribution and larger volume-weighted average particle size compared to Pt/C (Figure S15 and Table S1). The specific activity (SA) of PtCo, $Ga_{0.1}$ -PtCo, Ga-PtCo, and commercial Pt/C were accordingly calculated to be 3.54 ± 0.20 , 5.85 ± 0.38 , 4.74 ± 0.16 , and $0.59 \pm 0.08 \text{ mA cm}_{Pt}^{-2}$, respectively (Fig. 4b). The higher SA of $Ga_{0.1}$ -PtCo over Ga-PtCo and PtCo was contributed to the smaller lattice constant of de-alloyed $Ga_{0.1}$ -PtCo (Figure S11), which resulted in a larger compressive strain on the Pt shells and thus promoted ORR kinetics^{7,10,14}. The ORR performance of Ga doped or undoped PtFe and PtNi were also studied (Figure S16, Figure S17). The SA of Ga-PtFe, PtFe, Ga-PtNi, and PtNi was tested to be 2.14 ± 0.13 , 1.52 ± 0.1 , 4.84 ± 0.15 , and $3.69 \pm 0.38 \text{ mA cm}_{Pt}^{-2}$, respectively. We noted that both Ga doped PtFe and PtNi with a higher ordering degree exhibited promoted SA compared to their undoped counterparts. We further calculated the MA

of the catalysts at 0.95 V to avoid the mass transport limited region³⁶. The MA at 0.95 V_{RHE} of $Ga_{0.1}$ -PtCo was calculated to be $0.345 \pm 0.010 \text{ A mg}_{Pt}^{-1}$, which is also much higher than that of Ga-PtCo ($0.209 \pm 0.015 \text{ A mg}_{Pt}^{-1}$), PtCo ($0.147 \pm 0.014 \text{ A mg}_{Pt}^{-1}$), and commercial Pt/C ($0.071 \pm 0.003 \text{ A mg}_{Pt}^{-1}$) (Table S4).

We performed DFT calculations to further understand the enhanced ORR activity of the highly ordered $Ga_{0.1}$ -PtCo IMCs catalyst. The structure used for calculation was modeled by a slab composed of a fully ordered $L1_0$ Ga-PtCo or Al PtCo bottom layer that was fixed, and three top Pt layers that were relaxed, denoting as $L1_0$ Ga-PtCo@Pt and Al PtCo@Pt respectively. Unlike $L1_0$ Ga-PtCo@Pt and Pt, the lattice constant of Al PtCo@Pt was derived from the high-temperature structure of random PtCo above T_c . Thus, the lattice constant of Al PtCo@Pt was simulated by ab initio molecular dynamics (Figure S18). More details can be found in the Calculation Method section. The DFT calculations revealed that the potential determining step (PDS) of all the three catalysts was the step to form OOH^* from OO^* with the energy barrier of 0.88, 0.97, and 1.06 eV for $L1_0$ Ga-PtCo@Pt, Al PtCo@Pt, and Pt, respectively (Fig. 4c). Considering the three-layer Pt shells of the catalysts, the strain effect instead of ligand effect was believed to be the main reason for the changes of electronic structure and ORR activity⁸. We further found a clear correlation between the lattice strain, the d-band center, and the ORR energy barrier: the $L1_0$ Ga-PtCo@Pt showed the lowest d-band center and the largest compressive strain, and thus the highest ORR activity (Fig. 4d, e).

The post-treated $Ga_{0.1}$ -PtCo sample was used as the cathode catalyst of MEA to demonstrate the practical application in PEMFCs (Fig. 5a, b). For comparison, the commercial 30 wt% Pt/C (TKK) cathode was also tested under the same conditions. In H_2 - O_2 single-cell test, the MA at 0.9 V of $Ga_{0.1}$ -PtCo achieved $1.07 \text{ A mg}_{Pt}^{-1}$, which was higher than that of Pt/C ($0.41 \text{ A mg}_{Pt}^{-1}$) and the US Department of Energy (DOE) 2025 target ($0.44 \text{ A g}_{Pt}^{-1}$)⁴. The polarization curve was

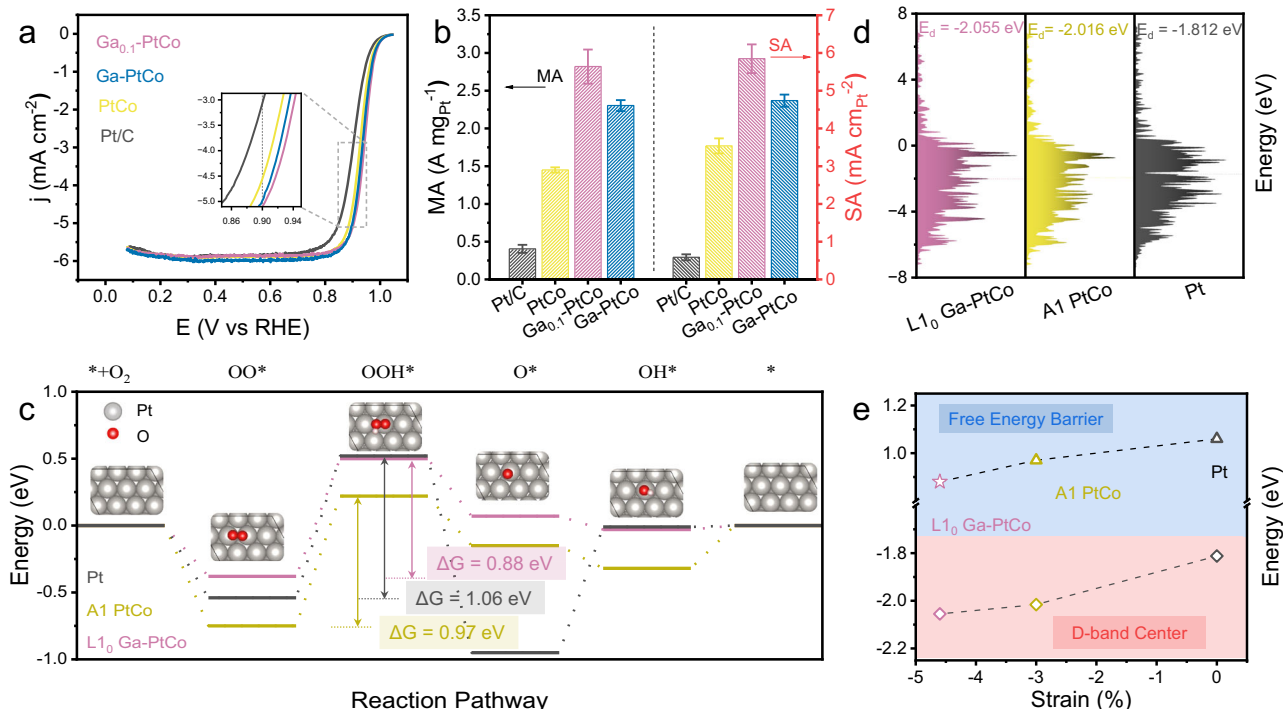


Fig. 4 | Electrochemical performance of Ga-doped PtCo. **a** ORR polarization curve of $\text{Ga}_{0.1}\text{-PtCo}$, Ga-PtCo , PtCo , and commercial Pt/C in O_2 -saturated 0.1 M HClO_4 . The insert shows the enlarged polarization curves at around 0.9 V. **b** MA and SA of the catalysts at 0.9 V. The error bar was obtained by three parallel experiments.

c Theoretical free energy diagram for L_{10} Ga-PtCo , A1 PtCo , and Pt based on a three layers Pt shell model from DFT at $U = 1.23$ V. **d** D-band center of L_{10} Ga-PtCo , A1 PtCo , and Pt . **e** Relation between strain, d band center, and ORR free energy barrier of L_{10} Ga-PtCo , A1-PtCo , and Pt .

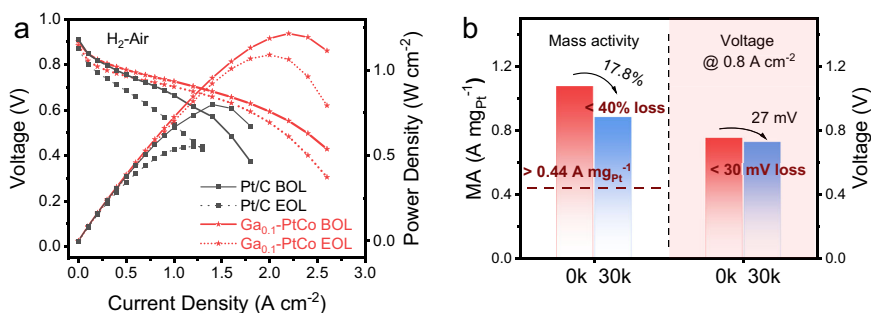


Fig. 5 | MEA performance of post-treated $\text{Ga}_{0.1}\text{-PtCo}$. **a** H_2 -air single-cell polarization curves and power density plots of the $\text{Ga}_{0.1}\text{-PtCo}$ and Pt/C cathodes before (BOL) and after (EOL) AST test. Test conditions: cathode loading of $0.075 \text{ mg}_{\text{Pt}} \text{ cm}^{-2}$.

cm^{-2} , 80°C , 100% relative humidity, $150 \text{ kPa}_{\text{abs, outlet}}$; H_2 and air flow rates were fixed at 0.5 and 2.0 liters min^{-1} , respectively. **b** MA at 0.9 V in $\text{H}_2\text{-O}_2$ fuel cells and the voltage at 0.8 A cm^{-2} in H_2 -air fuel cells before and after AST test.

also conducted under H_2/Air conditions, in which the peak power density of the MEA made with $\text{Ga}_{0.1}\text{-PtCo}$ cathode was 1200 mW cm^{-2} at 0.55 V with a low Pt loading of $0.075 \text{ mg}_{\text{Pt}} \text{ cm}^{-2}$, outperforming the Pt/C cathode (800 mW cm^{-2}). The H_2 -air fuel cell performance of the Ga-PtCo cathode was slightly lower than that of $\text{Ga}_{0.1}\text{-PtCo}$ cathode at high voltage region (Figure S19), owing to the lower ORR activity of the Ga-PtCo catalyst (Fig. 4a, b).

After 30,000 cycles of accelerated stress test (AST) from 0.6 to 0.95 V under H_2/N_2 , the $\text{Ga}_{0.1}\text{-PtCo}$ cathode still maintained a high MA of $0.88 \text{ A mg}_{\text{Pt}}^{-1}$ with a loss of 17.8%, which meets well the DOE stability target of less than 40% MA loss. The voltage loss of the MEA made with $\text{Ga}_{0.1}\text{-PtCo}$ cathode was 27 mV at 0.8 A cm^{-2} after 30,000 AST cycles, also meeting the DOE 2025 target (<30 mV loss). Further, a chronoamperometric test at a voltage of 0.6 V was conducted to evaluate the long-term durability of the $\text{Ga}_{0.1}\text{-PtCo}$ cathode. The current density of the $\text{Ga}_{0.1}\text{-PtCo}$ cathode dropped by 10% in 100 hours (Figure S20), which could be associated to the accumulation of dissolved Ga or Co cations contaminant in cathode catalyst layer. Continuous

accumulation of dissolved metal cations in the chronoamperometric test could result in increased mass transport resistance and thus performance degradation³⁷. Furthermore, the low-Pt $\text{Ga}_{0.1}\text{-PtCo}$ cathode exhibited a high rated power density of 1.05 W cm^{-2} at 0.67 V performed at 94°C and $250 \text{ kPa}_{\text{abs}}$ (Figure S21). The high-current-density performance is highly dependent on the transport properties of the cathode catalyst layer, which are controlled by the thickness of the catalyst layer³⁸, the ionomer distribution^{39–41}, the Pt roughness factor², carbon support type⁴², the Pt nanoparticle location⁴³, as well as the adopted test conditions^{39,44} (such as gas flow rate, backpressure, relative humidity, etc.). Systematical optimization of these parameters would significantly promote the transport properties of the catalyst layer and thus improve the H_2 -air fuel cell performance at high current density in the future.

Discussion

In summary, we have demonstrated a low-melting-point metal doping strategy for the synthesis of carbon-supported highly ordered

intermetallic M-PtCo catalysts. The ordering degree of the prepared M-PtCo catalysts was inversely correlated with the melting point of the doped M. We understood by experimental and theoretic studies that the doping of low-melting-point metal could greatly decrease the energy barrier of atom diffusion for atom ordering and thus promote the ordering degree. The Ga_{0.1}PtCo catalyst with a high ordering degree of 62% exhibited a large MA and rated power density with a low-Pt loading in PEMFCs. Our results highlight the general validity of low melting point metal doping in the control of phase transition kinetics by decreasing the diffusion barrier, which can further guide the synthesis of diverse intermetallics for fuel cells and other catalysis applications.

Methods

Synthesis of the M-PtCo, Ga-PtNi, and Ga-PtFe IMCs catalysts

Carbon-supported LL_o-type M-PtCo, Ga-PtNi, and Ga-PtFe IMCs catalysts were prepared by a conventional wet-impregnation method. For M-PtCo, a certain amount of H₂PtCl₆·(H₂O)₆, CoCl₂·6H₂O, and the salt of doped metal were added to the mixture of 100 mg Ketjenblack EC-600J and 60 mL ultrapure water (18.2 MΩ). The total metal content was controlled to be 20 wt%. The mixture was treated with ultrasound for 2 h and stirred for 8 h to get a homogenous solution before drying by rotary evaporation. Finally, the dried precursor was placed in a tube furnace and treated at 1000 °C for 2 h (heating rate, 5 °C/min) in Ar/H₂ (95:5) atmosphere to be fully alloyed and then cooling to room temperature with the furnace. The synthesis of LL_o Ga-PtFe and Ga-PtNi were in the same way as M-PtCo.

Characterization

The XRD patterns were analyzed using a Japan Rigaku DMax-γA rotation anode x-ray diffractometer. The wavelength used in XRD is 1.54178 Å by graphite monochromatized Cu-K radiation. HAADF-STEM images and aberration-corrected HAADF-STEM images were obtained on FEI Talos F200X and JEM ARM200F (S) TEM, respectively, with an accelerating voltage of 200 kV. EDS mapping and line-scanning were carried out using the Super X-EDS system of FEI Talos F200X.

Ordering degree calculation

The ordering degree was estimated by comparing the normalized intensity of the (110) peak to the sum of the intensities of the (111) and (200) peaks between the experimental XRD patterns and standard Powder Diffraction File cards of LL_o-PtCo. The calculation formula is as follows:

$$\text{Ordering degree (\%)} = \frac{S_{(110)}^{\text{exp}}}{S_{(111)+(200)}^{\text{exp}}} \bigg/ \frac{I_{(110)}^{\text{PDF}}}{I_{(111)+(200)}^{\text{PDF}}} * 100\% \quad (1)$$

$S_{(110)}^{\text{exp}}$, $S_{(111)+(200)}^{\text{exp}}$ is the integrated area under (110) peak and the sum of integrated area under (111) and (200) peak of the experimental XRD pattern, respectively. $I_{(110)}^{\text{PDF}}$, $I_{(111)+(200)}^{\text{PDF}}$ is the intensity at (110) peak and the sum of the intensity at (111) and (200) peak of the Powder Diffraction File, respectively.

Calculation methods

The plane-wave technique with a 500 eV cutoff was used for all spin-polarized DFT calculations^{45,46}, by the Vienna Ab-initio Simulation Package (VASP) codes 5.4⁴⁷. The projected enhanced wave method (PAW)^{48,49}, and revised Perdew–Burke–Ernzerho (RPBE) exchange-correlation functional⁵⁰ were used in the calculations. Spin-polarized calculations were carried out on all surfaces, the electron energy converged to 10⁻⁵ eV, and the force converged to 0.02 eV/Å. In the single crystal calculation, the transition states (TSS) were located by the climbing image nudged elastic band (CI-NEB) algorithm⁵¹. In order to maximize the order of the M-PtCo structure, 2 × 2 × 2 PtCo supercell was constructed, in which two Co atoms of sixteen atoms were replaced by M atoms in each supercell. Moreover, M atoms were

symmetrical with respect to the center of the supercell. For AIMD simulation, we performed 5 ps (2500 steps, two fs per step) within the canonical (NVT) ensemble at 1000 K to get an approximate stable structure. The Nose-Hoover thermostat is used in this simulation. Then 5 ps (2500 steps, two fs per step) within the isobaric-isothermic (NPT) ensemble to get reasonable lattice constants at the high temperature. The Langevin thermostat is used in this simulation with the default friction coefficient. (a separate friction coefficient for each of the NTYP atomic species found on the POTCAR-file.) For the ORR simulation, the calculated structure contained two relaxed layers and two layers fixed on the PtCo (111) surface and a 2 × 2 × 1 Monkhorst-Pack k-point mesh was used. The slab model used in our study was constructed based on our experimental results. As shown in Fig. 3d, a 3 atom-layers Pt shell can be observed for the the post-treated Ga_{0.1}PtCo catalyst. Thus, the calculated structure contained three Pt layers epitaxial growth on the PtCo (111) surface. Pt layer adjacent to the Ga_{0.1}PtCo core adopts a lattice parameter closer to that of the core, but outer two Pt shell layers relax towards the lattice constant of bulk Pt, which is known as strain relax^{7,52,53}. For the calculation of the Pt (111) system adsorption, two layers of metal are the most common calculation method⁵⁴. LL_o Ga-PtCo(111) is sliced from the ordered Ga-PtCo surface after DFT relaxed structure. Al-PtCo(111) is sliced from the disordered Ga-PtCo surface after DFT relaxed structure with Lattice Parameters from the average of MD process at 1000 K.

All periodic plate calculations were performed with a vacuum separation of at least 13 Å.

RDE electrochemical measurement

Electrochemical measurements were conducted by using CHI Instruments (CHI 760E) in a three-electrode electrochemical cell. Hg/Hg₂SO₄ with saturated K₂SO₄ solution and Pt foil served as the reference electrode and counter electrode, respectively. The reference electrode potential was calibrated to the reversible hydrogen electrode (RHE) potentials under H₂-saturated 0.1 M HClO₄ solution before tests.

Before the electrochemical test, the as-prepared supported M-PtCo catalysts were etched with 0.1 M HClO₄ in oil bath at 60 °C, followed by annealing at 400 °C for 2 h under Ar/H₂ to form the stable Pt-skin structure. For the preparation of the working electrode for RDE, 2 mg catalyst was dispersed in isopropanol (1.98 mL) and Nafion (20 μL). Then the mixture was stirred for 2 h and sonicated for 1 h to get a homogeneous ink. After that, a certain amount of the dispersion was dropped onto the rotating disk electrode (RDE, 0.196 cm²) and dried while rotating under ambient temperature. The loading of each catalyst on RDE is 15 μg_{metal} cm⁻².

All catalyst-coated electrodes were activated by a cyclic voltammetry (CV) method (scan rates of 250 mV s⁻¹ and potential ranges of 0.05–1.05 V vs. RHE) until the CV curves completely overlapped. Linear sweep voltammetry (LSV) measurements were then conducted in the O₂-saturated 0.1 M HClO₄ solution by sweeping the potential from 0.05 to 1.05 V at 10 mV s⁻¹ (1600 rpm). For each sample, all tests were repeated three times to get an error bar. For the electrochemical impedance spectroscopy (EIS) measurements, the frequency range was between 0.01 and 100,000 Hz, and initial voltage and amplitude voltage were set at 0.05 and 0.005 V (vs. RHE), respectively. The electrochemical active surface area (ECSA) was obtained by CO stripping test. CO stripping test was conducted by bubbling CO into 0.1 M HClO₄ electrolyte for 20 min with holding electrode potential at 0.05 V, followed by bubbling N₂ into the electrolyte for 30 min to remove unadsorbed CO in the electrolyte. Then cyclic voltammetry (CV) curve was collected by scanning from 0.05 V to 1.05 V at a scanning rate of 50 mV/s. The ECSA was calculated accordingly:

$$\text{ECSA} = \frac{S_{\text{CO}}}{0.42 \times v_{\text{scan}} \times m_{\text{Pt}}} \quad (2)$$

where S_{CO} , v_{scan} , and m_{Pt} represent the integral area of CO stripping, scan speed, and Pt loading, respectively.

MEA test

For the preparation of the MEA for PEMFCs, a certain amount of catalyst was dispersed in the mixture of isopropanol and water (1:1). After sonication dispersion, D2020® perfluorosulfonic acid (PFSA) with an equivalent weight of 950 g mol^{-1} was added with the ratio of ionomer to carbon (I/C) of 0.9. The catalyst concentration was controlled to be 2.5 mg mL^{-1} . Then the mixture was stirred for 2 h and sonicated for 2 h in the ice bath to get a homogeneous ink. The 5 cm^2 catalyst-coated-membrane (CCM) was prepared by ultrasonic spraying the homogeneous ink using a SonoTek ultrasonic spray coater at 48 kHz and 90°C on $12 \mu\text{m}$ GORE membrane to form $0.075 \text{ mg}_{\text{Pt}} \text{ cm}^{-2}$ cathode catalyst layer ($0.025 \text{ mg}_{\text{Pt}} \text{ cm}^{-2}$ for anode with 30 wt% TKK Pt/C). For the assembly of MEA, 215 μm GDL (22BB, SGL Carbon) and 140 μm gasket were used. The cell endplates were tightened with a torque of 10 Nm to achieve a desired compression of ~22%. Single cells were tested using a Scribner 850e fuel cell test stand. All MEA tests were measured in a 5 cm^2 single cell with a graphite flow field containing 7 flow channels in a serpentine arrangement⁵⁵. The pressure drop between the inlet and outlet of the cathode in the flow field under the H₂-Air test condition is less than 10 kPa (Table S5).

The MEA was initially activated by scan voltage method from the open circuit to 0.2 V till the polarization curve overlapped under the H₂/O₂ condition ($0.2/0.5 \text{ liters min}^{-1}$) at 80°C , 150 kPa_{abs}, and 100% relative humidity (RH). The MA was determined from H₂/O₂ polarization curve after iR-correction using HFR and H₂ crossover correction, and the standardized protocol to evaluate MA is shown in Table S6. The H₂-Air polarization curve was conducted under 80°C , 150 kPa_{abs}, and 100% RH, with a gas flow rate of $0.5/2 \text{ liters min}^{-1}$ H₂/Air for the anode/cathode. Following the guidance of DOE, the accelerated stress test (AST) was carried out at 80°C , 100 kPa_{abs}, and 100% RH with H₂/N₂ flow of $0.2/0.075 \text{ liters min}^{-1}$ for the anode/cathode, including 30,000 cycles of square wave with each cycle holding the MEA at a voltage of 0.6 V for 3 s and then 0.95 V for 3 s. The voltage recovery treatment was conducted to eliminate the effect of contaminants before and after AST test⁵⁶. The rated power density is estimated by H₂-Air polarization curve at 94°C , 250 kPa_{abs}, and 100% RH.

Data availability

Relevant data supporting the key findings of this study are available within the article and the Supplementary Information file. All data presented in this study are available from the corresponding authors (H.-W.L. and Y.K.) upon request. Source data are provided in this paper.

References

1. Debe, M. K. Electrocatalyst approaches and challenges for automotive fuel cells. *Nature* **486**, 43–51 (2012).
2. Banham, D. & Ye, S. Current status and future development of catalyst materials and catalyst layers for proton exchange membrane fuel cells: an industrial perspective. *ACS Energy Lett.* **2**, 629–638 (2017).
3. Lohse-Busch, H. et al. Technology Assessment of a Fuel Cell Vehicle: 2017 Toyota Mirai. (2018). <https://doi.org/10.2172/1463251>.
4. US DOE. DOE Technical Targets for Polymer Electrolyte Membrane Fuel Cell Components. (2016). <https://www.energy.gov/eere/fuelcells/doe-technical-targets-polymer-electrolyte-membrane-fuel-cell-components>.
5. Gasteiger, H. A., Kocha, S. S., Sompalli, B. & Wagner, F. T. Activity benchmarks and requirements for Pt, Pt-alloy, and non-Pt oxygen reduction catalysts for PEMFCs. *Appl. Catal. B* **56**, 9–35 (2005).
6. Kongkanand, A. & Mathias, M. F. The priority and challenge of high-power performance of low-platinum proton-exchange membrane fuel cells. *J. Phys. Chem. Lett.* **7**, 1127–1137 (2016).
7. Strasser, P. et al. Lattice-strain control of the activity in dealloyed core-shell fuel cell catalysts. *Nat. Chem.* **2**, 454–460 (2010).
8. Hernandez-Fernandez, P. et al. Mass-selected nanoparticles of Pt_xY as model catalysts for oxygen electroreduction. *Nat. Chem.* **6**, 732–738 (2014).
9. Escudero-Escribano, M. et al. Tuning the activity of Pt alloy electrocatalysts by means of the lanthanide contraction. *Science* **352**, 73–76 (2016).
10. Yang, C.-L. et al. Sulfur-anchoring synthesis of platinum intermetallic nanoparticle catalysts for fuel cells. *Science* **374**, 459–464 (2021).
11. Cheng, Q. et al. High-loaded sub-6 nm Pt₁Co₁ intermetallic compounds with highly efficient performance expression in PEMFCs. *Energy Environ. Sci.* **15**, 278–286 (2022).
12. Wang, X. X. et al. Ordered Pt₃Co intermetallic nanoparticles derived from metal-organic frameworks for oxygen reduction. *Nano Lett.* **18**, 4163–4171 (2018).
13. Li, J. et al. Hard-magnet L1₀-CoPt nanoparticles advance fuel cell catalysis. *Joule* **3**, (2018).
14. Rößner, L. & Armbrüster, M. Electrochemical energy conversion on intermetallic compounds: a review. *ACS Catal.* **9**, 2018–2062 (2019).
15. Liang, J. et al. Tungsten-doped L1₀-PtCo ultrasmall nanoparticles as a high-performance fuel cell cathode. *Angew. Chem. Int. Ed.* **58**, 15471–15477 (2019).
16. Bu, L. et al. Biaxially strained PtPb/Pt core/shell nanoplate boosts oxygen reduction catalysis. *Science* **354**, 1410–1414 (2016).
17. Hodnik, N. et al. Effect of ordering of PtCu₃ nanoparticle structure on the activity and stability for the oxygen reduction reaction. *Phys. Chem. Chem. Phys.* **16**, 13610–13615 (2014).
18. Xiong, Y. et al. Revealing the atomic ordering of binary intermetallics using in situ heating techniques at multilength scales. *Proc. Natl Acad. Sci. USA* **116**, 1974–1983 (2019).
19. Song, T.-W. et al. Intermetallic PtFe electrocatalysts for the oxygen reduction reaction: ordering degree-dependent performance. *Small* **18**, 2202916 (2022).
20. Zeng, W.-J. et al. Phase diagrams guide synthesis of highly ordered intermetallic electrocatalysts: separating alloying and ordering stages. *Nat. Commun.* **13**, 7654 (2022).
21. Wang, D. et al. Structurally ordered intermetallic platinum-cobalt core-shell nanoparticles with enhanced activity and stability as oxygen reduction electrocatalysts. *Nat. Mater.* **12**, 81–87 (2013).
22. Yan, Y. et al. Intermetallic nanocrystals: syntheses and catalytic applications. *Adv. Mater.* **29**, (2017).
23. Kitakami, O., Shimada, Y., Oikawa, K., Daimon, H. & Fukamichi, K. Low-temperature ordering of L1₀-CoPt thin films promoted by Sn, Pb, Sb, and Bi additives. *Appl. Phys. Lett.* **78**, 1104–1106 (2001).
24. Yan, Q. et al. Enhanced chemical ordering and coercivity in FePt alloy nanoparticles by Sb-doping. *Adv. Mater.* **17**, 2233–2237 (2005).
25. Maeda, T., Kai, T., Kikitsu, A., Nagase, T. & Akiyama, J.-i. Reduction of ordering temperature of an FePt-ordered alloy by addition of Cu. *Appl. Phys. Lett.* **80**, 2147–2149 (2002).
26. Kang, S., Harrell, J. W. & Nikles, D. E. Reduction of the fcc to L1₀ ordering temperature for self-assembled FePt nanoparticles containing Ag. *Nano Lett.* **2**, 1033–1036 (2002).
27. Hu, M. et al. MOF-confined sub-2 nm atomically ordered intermetallic PdZn nanoparticles as high-performance catalysts for selective hydrogenation of acetylene. *Adv. Mater.* **30**, 1801878 (2018).
28. Alloyeau, D. et al. Size and shape effects on the order-disorder phase transition in CoPt nanoparticles. *Nat. Mater.* **8**, 940–946 (2009).

29. Chen, M. et al. Kinetics, energetics, and size dependence of the transformation from Pt to ordered PtSn intermetallic nanoparticles. *Nanoscale* **11**, 5336–5345 (2019).
30. Choi, H., Ko, J.-H., Kim, Y.-H. & Jeong, S. Steric-Hindrance-driven shape transition in PbS quantum dots: understanding size-dependent stability. *J. Am. Chem. Soc.* **135**, 5278–5281 (2013).
31. Jia, Q. et al. Roles of Mo surface dopants in enhancing the ORR performance of octahedral PtNi nanoparticles. *Nano Lett.* **18**, 798–804 (2018).
32. Zeng, W.-J. et al. Alloying matters for ordering: synthesis of highly ordered PtCo intermetallic catalysts for fuel cells. *Inorg. Chem.* **62**, 5262–5269 (2023).
33. Han, B. et al. Record activity and stability of dealloyed bimetallic catalysts for proton exchange membrane fuel cells. *Energy Environ. Sci.* **8**, 258–266 (2015).
34. Lide D. *CRC Handbook of chemistry and physics*. CRC Press (2007); **8**.
35. Han, B., Carlton, C. E., Suntivich, J., Xu, Z. & Shao-Horn, Y. Oxygen reduction activity and stability trends of bimetallic Pt_{0.5}M_{0.5} nanoparticle in acid. *J. Phys. Chem. C* **119**, 3971–3978 (2015).
36. Huang, X. et al. High-performance transition metal-doped Pt₃Ni octahedra for oxygen reduction reaction. *Science* **348**, 1230–1234 (2015).
37. Ramaswamy, N. et al. High-current density durability of Pt/C and PtCo/C catalysts at similar particle sizes in PEMFCs. *J. Electrochem. Soc.* **168**, 024519 (2021).
38. Sassin, M. B., Garsany, Y., Atkinson, R. W., Hjelm, R. M. E. & Swider-Lyons, K. E. Understanding the interplay between cathode catalyst layer porosity and thickness on transport limitations en route to high-performance PEMFCs. *Int. J. Hydrog. Energy* **44**, 16944–16955 (2019).
39. Liu, Y. et al. Proton conduction and oxygen reduction kinetics in PEM fuel cell cathodes: effects of ionomer-to-carbon ratio and relative humidity. *J. Electrochem. Soc.* **156**, B970 (2009).
40. Ott, S. et al. Ionomer distribution control in porous carbon-supported catalyst layers for high-power and low Pt-loaded proton exchange membrane fuel cells. *Nat. Mater.* **19**, 77–85 (2020).
41. Ramaswamy, N., Gu, W., Ziegelbauer, J. M. & Kumaraguru, S. Carbon support microstructure impact on high current density transport resistances in PEMFC cathode. *J. Electrochem. Soc.* **167**, 064515 (2020).
42. Liu, Y., Ji, C., Gu, W., Jorne, J. & Gasteiger, H. A. Effects of catalyst carbon support on proton conduction and cathode performance in PEM fuel cells. *J. Electrochem. Soc.* **158**, B614 (2011).
43. Ito, T. et al. Three-dimensional spatial distributions of Pt catalyst nanoparticles on carbon substrates in polymer electrolyte fuel cells. *Electrochemistry* **79**, 374–376 (2011).
44. Zhang, J., Song, C., Zhang, J., Baker, R. & Zhang, L. Understanding the effects of backpressure on PEM fuel cell reactions and performance. *J. Electroanal. Chem.* **688**, 130–136 (2013).
45. Hohenberg, P. & Kohn, W. Inhomogeneous electron gas. *Phys. Rev.* **136**, B864–B871 (1964).
46. Kohn, W. & Sham, L. J. Self-consistent equations including exchange and correlation effects. *Phys. Rev.* **140**, A1133–A1138 (1965).
47. Kresse, G. & Furthmüller, J. Efficient iterative schemes for ab initio total-energy calculations using a plane-wave basis set. *Phys. Rev. B* **54**, 11169–11186 (1996).
48. Blöchl, P. E. Projector augmented-wave method. *Phys. Rev. B Condens* **50**, 17953–17979 (1994).
49. Kresse, G. & Joubert, D. From ultrasoft pseudopotentials to the projector augmented-wave method. *Phys. Rev. B* **59**, 1758–1775 (1999).
50. Hammer, B., Hansen, L. B. & Nørskov, J. K. Improved adsorption energetics within density-functional theory using revised Perdew-Burke-Ernzerhof functionals. *Phys. Rev. B* **59**, 7413–7421 (1999).
51. Henkelman, G., Uberuaga, B. P. & Jónsson, H. A climbing image nudged elastic band method for finding saddle points and minimum energy paths. *J. Chem. Phys.* **113**, 9901–9904 (2000).
52. Wang, J. X. et al. Oxygen reduction on well-defined core-shell nanocatalysts: particle size, facet, and Pt shell thickness effects. *J. Am. Chem. Soc.* **131**, 17298–17302 (2009).
53. Fusy, J., Menaucourt, J., Alnot, M., Huguot, C. & Ehrhardt, J. J. Growth and reactivity of evaporated platinum films on Cu(111): a study by AES, RHEED and adsorption of carbon monoxide and xenon. *Appl. Surf. Sci.* **93**, 211–220 (1996).
54. Greeley, J. et al. Alloys of platinum and early transition metals as oxygen reduction electrocatalysts. *Nat. Chem.* **1**, 552–556 (2009).
55. Simon, C., Hasché, F., Müller, D. & Gasteiger, H. A. Influence of the gas diffusion layer compression on the oxygen mass transport in PEM fuel cells. *ECS Trans.* **69**, 1293 (2015).
56. Kabir, S. et al. Elucidating the dynamic nature of fuel cell electrodes as a function of conditioning: an ex situ material characterization and in situ electrochemical diagnostic study. *ACS Appl. Mater. Interfaces* **11**, 45016–45030 (2019).

Acknowledgements

We acknowledge the funding support from the National Key Research and Development Program of China (Grant 2018YFA0702001 and 2021YFA1200103), the National Natural Science Foundation of China (Grant 22071225 and 22221003), the Plan for Anhui Major Provincial Science & Technology Project (Grant 202203a0520013 and 2021d05050006), the Fundamental Research Funds for the Central Universities (Grant WK2060190103), the Joint Funds from Hefei National Synchrotron Radiation Laboratory (Grant KY2060000175), Collaborative Innovation Program of Hefei Science Center of CAS (Grant 2021HSC-CIP015), and USTC Research Funds of the Double First-Class Initiative. The numerical calculations in this paper have been done on the super-computing system in the Supercomputing Center of the University of Science and Technology of China.

Author contributions

H.-W.L., R.-Y.S., and X.-C.X. conceived and designed the project. R.-Y.S., X.-C.X., Z.-H.Z. synthesized and characterized the catalysts. X.-C.X., W.-J.Z., T.-W.S., P.Y., and L.T. studied the electrochemical performance. A.L. and C.-S.M. made the MEAs. Y.K. conducted the calculation. H.-W.L. and R.-Y.S. co-wrote the manuscript. All the authors discussed the results and commented on the manuscript.

Competing interests

The authors declare no competing interests.

Additional information

Supplementary information The online version contains supplementary material available at <https://doi.org/10.1038/s41467-023-41590-2>.

Correspondence and requests for materials should be addressed to Yuan Kong or Hai-Wei Liang.

Peer review information *Nature Communications* thanks the anonymous reviewer(s) for their contribution to the peer review of this work. A peer review file is available.

Reprints and permissions information is available at <http://www.nature.com/reprints>

Publisher's note Springer Nature remains neutral with regard to jurisdictional claims in published maps and institutional affiliations.

Open Access This article is licensed under a Creative Commons Attribution 4.0 International License, which permits use, sharing, adaptation, distribution and reproduction in any medium or format, as long as you give appropriate credit to the original author(s) and the source, provide a link to the Creative Commons licence, and indicate if changes were made. The images or other third party material in this article are included in the article's Creative Commons licence, unless indicated otherwise in a credit line to the material. If material is not included in the article's Creative Commons licence and your intended use is not permitted by statutory regulation or exceeds the permitted use, you will need to obtain permission directly from the copyright holder. To view a copy of this licence, visit <http://creativecommons.org/licenses/by/4.0/>.

© The Author(s) 2023